

## FAST drift scan survey for H<sub>I</sub> intensity mapping: simulation on Bayesian-stacking-based H<sub>I</sub> mass function estimation

JIAOXIN WANG <sup>1</sup>, YICHAO LI <sup>1</sup>, HENGXING PAN <sup>2</sup>, FUREN DENG <sup>2,3,4,5</sup>, DIYANG LIU <sup>1</sup>, WENXIU YANG <sup>2,3</sup>, WENKAI HU <sup>6,7</sup>,  
YOUANG WANG <sup>2,3,4,1</sup>, XIN ZHANG <sup>1,8,9</sup> AND XUELEI CHEN <sup>2,1,4,3</sup>

<sup>1</sup>Key Laboratory of Cosmology and Astrophysics (Liaoning) & College of Sciences, Northeastern University, Shenyang 110819, China

<sup>2</sup>National Astronomical Observatories, Chinese Academy of Sciences, Beijing 100101, China

<sup>3</sup>School of Astronomy and Space Science, University of Chinese Academy of Sciences, Beijing 100049, China

<sup>4</sup>Key Laboratory of Radio Astronomy and Technology, Chinese Academy of Sciences, A20 Datun Road, Chaoyang District, Beijing 100101, China

<sup>5</sup>Institute of Astronomy, University of Cambridge, Madingley Road, Cambridge, CB3 0HA, UK

<sup>6</sup>Department of Physics & Astronomy, University of the Western Cape, Cape Town 7535, South Africa

<sup>7</sup>ARC Centre of Excellence for All Sky Astrophysics in 3 Dimensions (ASTRO 3D), Australia

<sup>8</sup>National Frontiers Science Center for Industrial Intelligence and Systems Optimization, Northeastern University, Shenyang 110819, China

<sup>9</sup>Key Laboratory of Data Analytics and Optimization for Smart Industry (Ministry of Education), Northeastern University, Shenyang 110819, China

### ABSTRACT

This study investigates the estimation of the neutral hydrogen (H<sub>I</sub>) mass function (H<sub>I</sub>MF) using a Bayesian stacking approach with simulated data for the Five-hundred-meter Aperture Spherical radio Telescope (FAST) H<sub>I</sub> intensity mapping (H<sub>I</sub>IM) drift-scan surveys. Using data from the IllustrisTNG simulation, we construct H<sub>I</sub> sky cubes at redshift  $z \sim 0.1$  and the corresponding optical galaxy catalogs, simulating FAST observations under various survey strategies, including pilot, deep-field, and ultradeep-field surveys. The H<sub>I</sub>MF is measured for distinct galaxy populations – classified by optical properties into red, blue, and bluer galaxies – and injected with systematic effects such as observational noise and flux confusion caused by the FAST beam. The results show that Bayesian stacking significantly enhances H<sub>I</sub>MF measurements. For red and blue galaxies, the H<sub>I</sub>MF can be well constrained with pilot surveys, while deeper surveys are required for the bluer galaxy population. Our analysis also reveals that sample variance dominates over observational noise, emphasizing the importance of wide-field surveys to improve constraints. Furthermore, flux confusion shifts the H<sub>I</sub>MF toward higher masses, which we address using a transfer function for correction. Finally, we explore the effects of intrinsic sample incompleteness and propose a framework to quantify its impact. This work lays the groundwork for future H<sub>I</sub>MF studies with FAST H<sub>I</sub>IM, addressing key challenges and enabling robust analyses of H<sub>I</sub> content across galaxy populations.

*Keywords:* Large-scale structure of the universe (902) — Galaxy evolution (594) — Extragalactic astronomy (506) — Surveys (1671) — Bayesian statistics (1900)

### 1. INTRODUCTION

Neutral hydrogen (H<sub>I</sub>) is the most abundant element in the Universe and plays an important role in exploring the evolution of the Universe. The distribution of H<sub>I</sub> content in galaxies is represented by the H<sub>I</sub> mass function (H<sub>I</sub>MF), which is defined as the number density of galaxies as the function of H<sub>I</sub> mass. The measurement of H<sub>I</sub>MF across cosmic time is critical for understanding galaxy formation and evolution.

The H<sub>I</sub>MF has been measured within the local Universe via the H<sub>I</sub> galaxy surveys, e.g. the H<sub>I</sub> Parkes All-Sky Survey (HIPASS; Barnes et al. 2001; Zwaan et al. 2005) and the Arecibo Legacy Fast ALFA survey (ALFALFA survey; Gio-

Corresponding author: Yichao Li  
liyichao@mail.neu.edu.cn

Corresponding author: Xin Zhang  
zhangxin@mail.neu.edu.cn

Corresponding author: Xuelei Chen  
xuelei@cosmology.bao.ac.cn

vanelli et al. 2005; Martin et al. 2010; Jones et al. 2018), which are conducted with the Parkes telescope and the Arecibo telescope, respectively. A few deeper blind H<sub>I</sub> galaxy surveys are currently in progress, which target to measure the HiMF to the faint-end and higher redshift using the newly constructed or upgraded radio telescopes. For instance, the Australian Square Kilometre Array Pathfinder (ASKAP; Johnston et al. 2007; DeBoer et al. 2009) has carried out the Widefield ASKAP L-band Legacy All-sky Blind Survey (WALLABY; Koribalski et al. 2020) and the Deep Investigation of Neutral Gas Origin (DINGO; Rhee 2020); the Netherlands Aperture Tile In Focus (AperTIF; Verheijen et al. 2009; Oosterloo et al. 2009) which is a phase-array-feed (PAF) upgrade to the Westerbork Synthesis Radio Telescope (WSRT), is conducting the H<sub>I</sub> galaxy imaging survey (Verheijen et al. 2009); and the Meer Karoo Array Telescope (MeerKAT; Jonas 2009) carries out the MeerKAT International GHz Tiered Extragalactic Exploration (MIGHTEE) survey (Jarvis et al. 2016) and the Looking At the Distant Universe with the MeerKAT Array (LADUMA) survey (Holwerda et al. 2012; Blyth et al. 2016).

The Five-hundred-meter Aperture Spherical radio Telescope (FAST, Nan et al. 2011; Li & Pan 2016) is the largest single-dish radio telescope in the world. It has an effective aperture of 300 meters and is equipped with a multi-beam feed system and low-noise cryogenic receivers (Jiang et al. 2020). H<sub>I</sub> galaxy survey is one of the primary scientific focuses for FAST. FAST All Sky H<sub>I</sub> (FASHI) is one of the FAST H<sub>I</sub> survey projects, which is proposed to cover the entire sky that can be detected by FAST telescope, ranging a declination of  $-14^\circ$  to  $+66^\circ$  (Zhang et al. 2024). The Commensal Radio Astronomy FasT Survey (CRAFTS; Li et al. 2018) is simultaneously conducting the surveys for pulsar and fast radio burst search, the Galactic H<sub>I</sub>, and the extragalactic galaxies (Zhang et al. 2019). Recently, Ma et al. (2024) presented a complete measurement of HiMF by combining the H<sub>I</sub> catalogs from HIPASS, ALFALFA, and FASHI surveys.

HiMF measurement with galaxy surveys beyond the local Universe is currently sensitivity-limited. The next-generation telescope, such as the Square Kilometer Array (SKA)<sup>1</sup> (Santos et al. 2015; Square Kilometre Array Cosmology Science Working Group et al. 2020), has the potential to explore the HiMF across a wide redshift range. On the other hand, a promising approach to break the flux limit and improving the signal-to-noise relies on the stacking technique, which combines the flux measurements from the H<sub>I</sub> survey and precise positional information from another survey, particularly galaxy surveys in the optical band. By co-adding the spectral line data at the known locations of many galaxies, the stacking

analysis leads to an enhancement of the signal-to-noise ratio (Delhaize et al. 2013; Rhee et al. 2018).

The stacking technique is also beneficial for HiMF measurements with H<sub>I</sub> intensity mapping (HiIM) surveys, which measures the total H<sub>I</sub> intensity of many galaxies within large voxels (Chang et al. 2008; Loeb & Wyithe 2008; Mao et al. 2008; Pritchard & Loeb 2008; Wyithe & Loeb 2008; Wyithe et al. 2008; Peterson et al. 2009; Bagla et al. 2010; Seo et al. 2010; Lidz et al. 2011; Ansari et al. 2012; Battye et al. 2013). The HiIM survey can be quickly carried out and extended to cosmological survey volume, which is ideal for cosmological investigations and exploring astrophysical processes over a broad cosmic time range. (Xu et al. 2015; Zhang et al. 2021; Jin et al. 2021; Wu & Zhang 2022; Wu et al. 2023; Wu et al. 2023; Zhang et al. 2023; Jin et al. 2020; Zhang et al. 2019; Pan et al. 2024). The HiIM was first explored with large radio telescope facilities, such as the Green Bank Telescope (GBT) and Parkes Telescope (Chang et al. 2010; Masui et al. 2013; Anderson et al. 2018; Wolz et al. 2017, 2022). Currently, there are several ongoing HiIM experiments focusing on the post-reionization epoch, such as the Tianlai project (Chen 2012; Li et al. 2020; Wu et al. 2021; Perdureau et al. 2022; Sun et al. 2022), the Canadian Hydrogen Intensity Mapping Experiment (CHIME, Bandura et al. 2014; Amiri et al. 2023). There are also some HiIM experiments which are under construction, such as the Baryonic Acoustic Oscillations from Integrated Neutral Gas Observations (BINGO, Battye et al. 2013) and the Hydrogen Intensity and Real-Time Analysis experiment (HIRAX, Newburgh et al. 2016). The HiIM technique is also proposed as the major cosmology project with SKA and MeerKAT (Bull et al. 2015; Santos et al. 2017; Li et al. 2021; Wang et al. 2021; Paul et al. 2021; Chen et al. 2023). Recently, the MeerKAT HiIM survey reported the cross-correlation power spectrum detection with the optical galaxy survey using single dish observation mode (Cunnington et al. 2023; MeerKLASS Collaboration et al. 2024; Carucci et al. 2024) and the auto power spectrum detection at Mpc scales using the MeerKAT interferometric observation mode (Paul et al. 2023). The HiIM auto power spectrum on large scales remains undetected (Switzer et al. 2013).

The HiIM can be carried out with FAST drift scan observation (Hu et al. 2020). The initial data analysis pipeline for FAST HiIM drift scan survey was investigated with pilot surveys, e.g., the Fast neuTRal HyDRogen intensity Mapping Experiment (FATHOMER, Li et al. 2023; Zhao et al. 2024; Liu et al. 2024) and H<sub>I</sub> cosmology projects with CRAFTS (Yang et al. 2024). In this study, we simulate the HiMF measurements for the FAST H<sub>I</sub> drift scan survey using a Bayesian-stacking-based approach, which was pioneered in the work of Pan et al. (2020) and further developed in Pan et al. (2021, 2024) for measuring the H<sub>I</sub> scaling relations.

<sup>1</sup> <https://www.skao.int>

The paper is organized as follows. In Section 2 we briefly introduce the simulation datasets used in this study, including the H I cube and the corresponding optical-selected galaxy sample. In Section 3 we introduce the Bayesian-stacking-based H I MF measurement method, the FAST observation effect simulation method, and the galaxy classification method. In Section 4 we show our results and discuss the implications; and summarize and conclude in Section 5. We use the standard  $\Lambda$ CDM cosmology with the Hubble constant  $h = 0.6774$ , total matter density  $\Omega_m = 0.3089$  and dark energy density  $\Omega_\Lambda = 0.6911$  (Planck Collaboration et al. 2016).

## 2. SIMULATION DATA

### 2.1. The TNG simulation

The H I cube is constructed using a snapshot of hydrodynamic simulation. We use the public hydrodynamic simulation data released by the IllustrisTNG project <sup>2</sup> (Nelson et al. 2019, hereafter TNG). The TNG project has three different data volumes, i.g. the TNG50, TNG100, and TNG300 corresponding to comoving volume of 35, 75, and 205  $h^{-3}\text{Mpc}^3$ , respectively. In this work, we adopt one snapshot of the TNG100 simulation box at the redshift of 0.1, which has the comoving volume suitable for our FAST H I M drift scan pilot survey. The threshold of  $2 \times 10^8 M_\odot$  for gas mass and stellar mass is applied to the simulation box following the analysis in the literature (Diemer et al. 2018). To ensure sample completeness, galaxies with either gas or stellar mass pass the threshold are considered reasonable galaxies.

### 2.2. H I sky cube simulation

The total neutral gas mass, including both the H I and H<sub>2</sub>, is provided by the TNG simulation. The TNG simulation utilizes different neutral gas models for the high-density and low-density regions, i.e., in the high-density regions, the neutral fraction is calculated considering the effects of cooling, heating, and ionization, while in the low-density regions, the gas is assumed to be in ionization equilibrium with a self-shielding effect against the time-evolving ultraviolet(UV)/X-ray background. In addition, the heating and ionization effect of stellar and active galactic nucleus (AGN) feedback is also coupled in the calculation. For a more detailed discussion, refer to the work of Diemer et al. (2018). The H I fraction is then determined according to the H<sub>2</sub> abundance following the model from Gnedin & Kravtsov (2011). For more details of the H I to H<sub>2</sub> fraction, refer to the work of Deng et al. (2022).

The TNG simulation box is then gridded into a sky cube with a pixel area of  $20 \times 20 \text{ kpc}^2$  and frequency resolution of 0.1 MHz. We use flat sky approximation with  $z$ -axis of the TNG simulation box as the line-of-sight (LoS) direction

and set the  $z$ -axis center as the comoving distance of redshift 0.1. The projected sky area is  $\sim 210 \text{ deg}^2$ , which is comparable to the currently FAST H I M drift scan pilot survey. The comoving distance of each particle is then converted to observer-frame frequency under the assumption of the  $\Lambda$ CDM cosmology model (Planck Collaboration et al. 2016). In addition, the LoS projection of the peculiar velocity for each particle is also considered to form a realistic galaxy H I emission line profile. The frequency of particles in the observer frame is calculated via,

$$\nu_{\text{obs}} = \frac{\nu_0}{1 + z + v_z/c}, \quad (1)$$

where  $\nu_{\text{obs}}$  is the particle's frequency at observer frame,  $z$  is the particle's cosmological redshift,  $\nu_0 = 1.42 \text{ GHz}$  is the H I rest-frame frequency,  $c$  is the speed of light, and  $v_z$  is the LoS projection of the particle's peculiar velocity.

The rest-frame velocity integrated H I flux of each particle is then calculated via (Meyer et al. 2017),

$$\left( \frac{S_{\text{H I}}}{\text{Jy Hz}} \right) \simeq \frac{1}{49.7} \left( \frac{m_{\text{H I}}}{h^{-2} M_\odot} \right) \left( \frac{d_L}{h^{-1} \text{Mpc}} \right)^{-2}, \quad (2)$$

where  $m_{\text{H I}}$  and  $d_L$  are the H I mass and luminosity distance of the particles, respectively. The flux of particles involved in the same pixel of the sky cube is then integrated. The pixel size and frequency resolution are fine enough to resolve both the galaxy image and the H I profile. The frequency slices of the simulated sky cube are shown in Figure 1.

### 2.3. The optical galaxy survey catalog

The optical galaxy survey catalog, which is required as the proxy for H I-stacking analysis, is also simulated using the corresponding galaxy sample of the TNG simulation. The survey area and available frequency range for FAST H I survey coincide with the galaxy catalog of Sloan Digital Sky Survey <sup>3</sup> (SDSS). In particular, the main galaxy sample (MGS) of the SDSS Data Release 7 (DR7; Abazajian et al. 2009) covers the redshift range  $0 < z < 0.2$ , which corresponds to the high-frequency band of the FAST H I survey. The MGS galaxy catalog occupies a footprint of  $\sim 6800 \text{ deg}^2$ . The MGS could be approximately constructed using magnitude cut,

$$14.5 < r_{\text{pet}} < 17.6, \quad (3)$$

where  $r_{\text{pet}}$  is the extinction-corrected  $r$ -band Petrosian magnitude (Ross et al. 2015).

The photometry measurements of the TNG galaxy samples are simulated using method similar to that of Deng et al. (2022), which adopte the synthetic stellar photometry model of Nelson et al. (2018). We use model B in Nelson et al. (2018)

<sup>2</sup> <https://www.tng-project.org>

<sup>3</sup> <https://www.sdss.org>

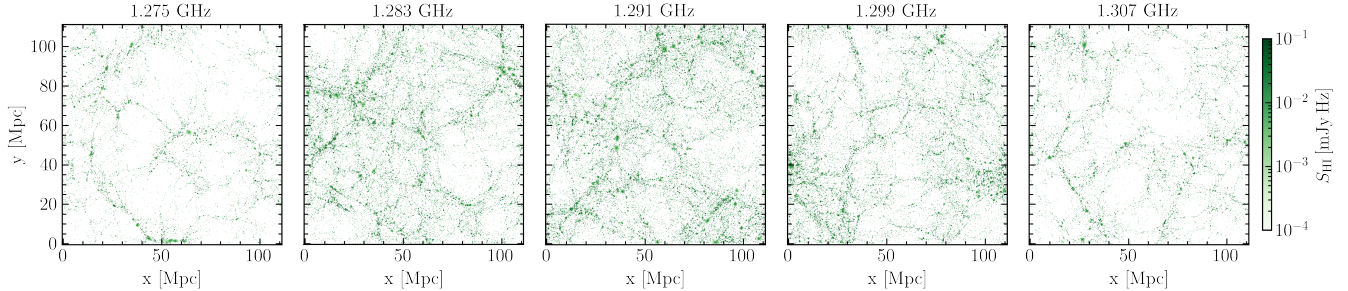


**Figure 1.** The H I flux distribution of simulated sky map at different frequencies integrated across a frequency range of 8.0 MHz.

**Table 1.** Comparing the galaxy number density of the catalogs generated by the TNG simulation with the observational catalog utilized in Dutta et al. (2020). The galaxy number densities are in units of  $h^3 \text{Mpc}^{-3}$ .

	Observational catalog	TNG simulation
Total	$1.23 \times 10^{-2}$	$0.97 \times 10^{-2}$
Red	$1.78 \times 10^{-3}$	$2.50 \times 10^{-3}$
Blue	$6.63 \times 10^{-3}$	$6.53 \times 10^{-3}$
Bluer	$6.47 \times 10^{-4}$	$6.69 \times 10^{-4}$

and calculate the spectrum of each particle via the stellar population synthesis code (Conroy et al. 2009; Conroy & Gunn 2010). The effect of dust obscuration is modeled using the dust component model of Charlot & Fall (2000). The galaxy spectrum is then convolved with SDSS instrumental bandpass to generate the corresponding apparent magnitude in the observational frame. Eventually, we apply a three-dimensional radial constraint of no more than 30 kpc from the subhalo center, which approximates a Petrosian aperture and yields an apparent magnitude similar to that utilized in MGS galaxy selection. For more details of the galaxy apparent magnitude simulation, refer to the work of Deng et al. (2022).

We apply the same apparent magnitude cut as the SDSS MGS galaxy catalog to the simulated TNG galaxy sample and restrict the redshift range between  $0.02 < z < 0.2$  to match the frequency range of the simulated H I sky cube.

In addition, following the data partition in the real observation data analysis (Dutta et al. 2020), we split the simulated MGS-like galaxy samples into three subsamples, i.e. the red, blue, and bluer galaxies. The detailed subsample classification method is presented in Section 3.5. The number density of galaxies in MGS-like sample, as well as the three subsamples, are listed in Table 1. We also list the galaxy number density of the same categories from the real observational data of Dutta et al. (2020) as the reference.

### 3. METHODS

#### 3.1. H I mass function

The H I MF represents the intrinsic number density of galaxies as a function of their H I mass. By definition the H I MF

can be expressed as (Rosenberg & Schneider 2002)

$$\Phi(M_{\text{HI}}) = \frac{dN_{\text{gal}}}{dV d \log_{10}(M_{\text{HI}})}, \quad (4)$$

where  $dN_{\text{gal}}$  represents the mean galaxy number in a comoving volume  $dV$ , where the galaxy H I mass falls inside a logarithmic mass bin centered on  $M_{\text{HI}}$ . In this work, we estimate the H I MF via Equation (4) with the full knowledge of the galaxy H I mass of the TNG simulation. It reflects the H I MF measurement via a highly sensitive H I galaxy survey and is denoted as  $\Phi_g(M_{\text{HI}})$ . We employ  $\Phi_g(M_{\text{HI}})$  as the proxy for the true H I MF and compare it to the H I MF estimated via the Bayesian stacking of the H I fluxes in the following analysis when considering different galaxy selection criteria.

The H I MF at redshift  $z$  can be fitted by the Schechter function (Zwaan et al. 2005; Martin et al. 2010),

$$\Phi(M_{\text{HI}}, z) = \ln(10) \Phi_* \left( \frac{M_{\text{HI}}}{M_*} \right)^{\alpha+1} e^{-\frac{M_{\text{HI}}}{M_*}} \left( 1 + z \right)^\beta, \quad (5)$$

where  $\Phi_*$  represents the normalization constant,  $M_*$  characterizes the ‘knee’ mass of the H I MF,  $\alpha + 1$  is the faint-end slope, and  $\beta$  represents the redshift evolution. The volume-weighted mean H I MF over a redshift range from  $z_1$  to  $z_2$  is defined as,

$$\Phi(M_{\text{HI}}, z_1, z_2) = \frac{1}{\tilde{V}} \int_{z_1}^{z_2} \frac{dV}{dz} \Phi(M_{\text{HI}}, z) dz, \quad (6)$$

where  $dV/dz$  is the differential comoving volume and  $\tilde{V} = \int_{z_1}^{z_2} dV$  is the normalization factor. In this work, the redshift evolution of the H I MF is ignored, and parameter  $\beta$  is fixed to  $\beta = 0$ . We use  $\Phi_*$ ,  $\alpha$ , and  $M_*$  as fitting parameters.

#### 3.2. Bayesian stacking measurements of H I MF

The key innovation of the Bayesian stacking method is directly estimating the H I MF using the galaxy number density function binned by measured flux. This method was explored in the previous work of Pan et al. (2020). We briefly summarize the basic procedures. We refer the interested readers to Pan et al. (2020) for more details.

The first step of the Bayesian stacking is to find a catalog of galaxies, which provide a proxy of galaxy locations. For

the HiMF measurement, typically an optical galaxy survey catalog can be used. In this work, as described in Section 2.3, we adopt a simulated galaxy catalog that mirrors the selection criteria of the SDSS main galaxy sample.

We then extract the flux measurements,  $S_m$ , from the pixels corresponding to the positions of optically identified galaxies. The galaxy number counts,  $k_i$ , for the  $i$ -th flux measurement interval,  $\Delta S_i = [S_i, S_i + \delta S]$ , are then determined from the radio survey. Instead of using uniform flux intervals, we employ the Bayesian Block method as proposed by Pan et al. (2020). This method dynamically determines optimal bin edges for the dataset using Bayesian statistics (Scargle et al. 2013; Astropy Collaboration et al. 2013, 2018). The Bayesian Block approach adaptively adjusts bin sizes to emphasize regions with significant variation while minimizing noise in sparser regions, resulting in more robust statistical constraints.

The measurement obtained from the above stacking analysis is the source count within a flux interval,  $\Psi(S_{\text{Hi}}) = dN/dS_{\text{Hi}}$ . If the noise can be ignored, the source count within the flux interval is related to the HiMF by,

$$\Psi(S_{\text{Hi}}) = \frac{dN}{dS_{\text{Hi}}} = \frac{1}{\ln(10)} \frac{\Phi(M_{\text{Hi}}, z_1, z_2)}{M_{\text{Hi}}} \frac{dM_{\text{Hi}}}{dS_{\text{Hi}}}, \quad (7)$$

where  $dM_{\text{Hi}}/dS_{\text{Hi}} = 2.35 \times 10^5 d_L^2 / (1+z)$  is derived from the conversation between galaxy Hi mass and its flux (Meyer et al. 2017),  $\Phi(M_{\text{Hi}}, z_1, z_2)$  is the Hi mass function defined with Equation (6). The posterior probability distribution of  $\Psi(S_{\text{Hi}})$ , as well as the fitting parameters involved in the HiMF model is propagated to the posterior probability distribution of the measurements via the Bayes' theorem,

$$P(\Psi(S_{\text{Hi}})|k_i) \propto P(k_i|\Psi(S_{\text{Hi}})) \quad (8)$$

We assume  $P(k_i|\Psi(S_{\text{Hi}}))$  obeys the Poisson distribution, and the probability function is expressed as,

$$P(k_i|\Psi(S_{\text{Hi}})) = \frac{\lambda_i^{k_i}}{k_i!} e^{-\lambda_i}, \quad (9)$$

where  $\lambda_i$  is the expectation value of the source number in the flux interval.

In actual observation, noise introduces additional flux and affects the source number counts  $k_i$ . Some galaxies may have weak Hi fluxes that fall below the noise variance. The expected value of the source number,  $\lambda_i$ , in the  $i$ -th flux interval is estimated by convolving the  $\Psi(S_{\text{Hi}})$  distribution with the noise distribution function,

$$\lambda_i = \int dS_{\text{Hi}} \left( \Psi(S_{\text{Hi}}) \int_{\Delta S_i} dS_m P_N(S_m - S_{\text{Hi}}) \right). \quad (10)$$

Given the measured flux  $S_m$  and Hi flux  $S_{\text{Hi}}$ ,  $P_N(S_m - S_{\text{Hi}})$  represents the distribution of flux difference raised by the

noise. We model the noise distribution as a zero-centered Gaussian with a variance of  $\sigma_{\text{noise}}^2$ ,

$$P_N(S_m - S_{\text{Hi}}) = \frac{1}{\sigma_{\text{noise}} \sqrt{2\pi}} \exp\left(-\frac{(S_m - S_{\text{Hi}})^2}{2\sigma_{\text{noise}}^2}\right). \quad (11)$$

Including the noise probability function,  $\lambda_i$  is expressed as,

$$\lambda_i = \int dS_{\text{Hi}} \frac{\Psi(S_{\text{Hi}})}{2} \left[ \text{erf}\left(\frac{S_i + \delta S - S_{\text{Hi}}}{\sqrt{2}\sigma_{\text{noise}}}\right) - \text{erf}\left(\frac{S_i - S_{\text{Hi}}}{\sqrt{2}\sigma_{\text{noise}}}\right) \right], \quad (12)$$

where the integration interval covers the full Hi flux range.

The likelihood function is constructed by combining the posterior distribution functions, as defined in Equation (9), across all flux intervals:

$$\mathcal{L} \propto \prod_i P(k_i|\Psi(S_{\text{Hi}})) = \prod_i \frac{\lambda_i^{k_i}}{k_i!} e^{-\lambda_i}, \quad (13)$$

where  $k_i$  represents the observables extracted from radio measurements. The fitting parameters involved in  $\lambda_i$  are constrained by maximizing the likelihood function. To explore the parameter space and posterior distributions, we use the multimodal nested sampling algorithm, MULTINEST<sup>4</sup> (Feroz et al. 2009).

### 3.3. FAST noise level

We consider the HiMF measurements uncertainty raised by the observation noise. Assuming the noise to be Gaussian, the noise level for a dual-polarization single-beam telescope observation can be well approximated by,

$$\sigma_{\text{noise}} = \sqrt{2} \frac{k_B T_{\text{sys}}}{A_{\text{eff}}} \frac{1}{\sqrt{\Delta\nu t}}, \quad (14)$$

where  $k_B$  is the Boltzmann constant,  $\Delta\nu$  is the frequency interval for a channel,  $A_{\text{eff}} \approx 50000 \text{ m}^2$  is the effective aperture area, and  $t$  is the total integration time. In this work, we assume the FAST HiMF survey is carried out with the drift scan observation mode. The integration time for one transit across one FAST beam is approximated by (Hu et al. 2020),

$$t_{\text{FWHM}} = \theta_B / (\omega_E \cos \delta), \quad (15)$$

where  $\theta_B$  represents the full-width-half-maximum beam width,

$$\theta_B = 2.94(1+z) \text{ arcmin}, \quad (16)$$

$\omega_E \approx 0.25 \text{ arcmin s}^{-1}$  is the angular velocity of the Earth rotation, and  $\delta$  is the Declination angle of the pointing direction. Assuming the drift scan pointing at the Zenith, where

<sup>4</sup> <https://github.com/JohannesBuchner/PyMultiNest>

**Table 2.** The FAST HiIM drift scan surveys considered in this work.

	Pilot survey	Deep-field survey	Ultradeep-field survey
$S_{\text{area}}^{\S}$	210 deg <sup>2</sup>	210 deg <sup>2</sup>	210 deg <sup>2</sup>
$n_{\text{repeat}}^{\dagger}$	1	4	8
$t_{\text{pix}}^{\ddagger}$	29 s	115 s	230 s

<sup>§</sup> The survey area

<sup>†</sup> The repeating times of the drift-scan observation

<sup>‡</sup> The integration time per pixel

$\delta \simeq 26$  deg, the integration time is about 14.4 s per beam at the redshift  $z \sim 0.1$  close to the mean redshift of the MGS-like galaxy samples.

During our FAST Hi drift scan *pilot survey*, the 19-feed array is employed and rotated by  $23.4^\circ$  to optimize the sky coverage. Taking into account the overlapping between the 19 beams, the sky can be scanned twice, i.e.  $t_{\text{pilot}} = 29$  s per drift-scan observation. A *deep-field survey* that repeats the drift scan four times on the same  $\sim 210$  deg<sup>2</sup> sky area will be examined in this work for FAST HiIM observations. An approximation for the integration time is  $t_{\text{deep}} = 115$  s. We'll also explore an *ultradeep-field survey*, which involves doing the drift scan on the same  $\sim 210$  deg<sup>2</sup> sky area eight times. Approximately  $t_{\text{ultra}} = 230$  s is the integration time. The HiIM drift scan surveys considered in this work are summarized in Table 2.

$T_{\text{sys}} = T_{\text{rec}} + T_{\text{sky}}$  is the system temperature, where  $T_{\text{rec}}$  is the receiver temperature and the sky temperature is modeled as (Hu et al. 2020),

$$T_{\text{sky}} = T_{\text{CMB}} + 25.2 \text{ K} \times (0.408/\nu_{\text{GHz}})^{2.75}, \quad (17)$$

where  $T_{\text{CMB}} = 2.73$  K is the mean temperature of the cosmic microwave background (CMB). The  $T_{\text{sys}} \sim 24$  K at the target frequencies. We adopt a slightly higher system temperature, following the system temperature estimation with FAST real data, to account for potentially extra noise contributions (Li et al. 2023).

### 3.4. Correction for the flux confusion effect

The FAST beam size is approximate via Equation (16), corresponding to the transverse comoving distance  $\sim 260 h^{-1}$  kpc at redshift  $z \simeq 0.1$ . The flux measurements could be confused since multiple galaxies may not be resolved (Hu et al. 2020). Such confusion effect should be corrected for HiMF estimation.

The FAST beam profile is modeled via a Gaussian function,

$$B(\theta) = \exp\left(-\frac{1}{2} \frac{\theta^2}{\sigma_B^2}\right), \quad (18)$$

where  $\sigma_B = \theta_B / (2\sqrt{2 \ln 2})$  is frequency dependent and  $\theta_B$  is the full-width-half-maximum defined in Equation (16).

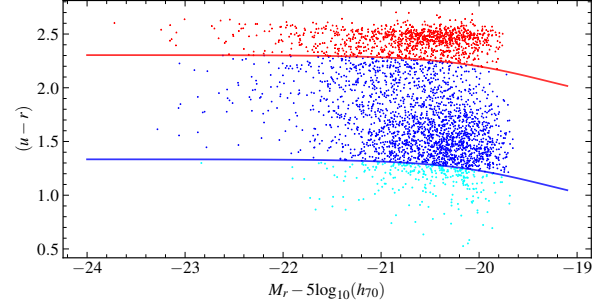


**Figure 2.** The color-magnitude space distribution of the galaxies from the simulated MGS catalog. The red curve shows the red/blue galaxy separator locus, which is defined with Equation (20), and the blue curve shows the separator for the blue/bluer galaxy. The red, blue, and bluer galaxies from the simulated MGS catalog are shown with the red, cyan, and blue scatter points, respectively.

The simulated sky cube is convolved with the beam function frequency-by-frequency. The Bayesian stacking analysis for the HiMF estimation is then applied to the beam-convolved sky cube. The transfer function for confusion correction is defined as the ratio of the beam-convolved HiMF,  $\Phi_B$ , to the reference HiMF,  $\Phi_{\text{ref}}$ ,

$$T_{\text{cc}} = \Phi_B / \Phi_{\text{ref}}, \quad (19)$$

where  $\Phi_{\text{ref}}$  is estimated by Bayesian-stacking the Hi flux extracted from the simulated galaxy catalog.

In this analysis, the flux leakage from the side lobe, as well as the shape variation between the 19 beams, are negligible compared to the flux measurement confusion raised from the beam smearing effect. However, the imperfect beam profile might complicate the foreground subtraction for HiIM survey and result in foreground residual contamination in the actual observations. We also ignore the foreground residual contamination and assume it can be further eliminated in future analysis (Ni et al. 2022; Gao et al. 2023).

### 3.5. Galaxy population

Understanding the relationship between the galaxy population and the distribution of Hi galaxies is essential to comprehending the evolution history of the galaxy. These investigations are now conducted using several Hi galaxy surveys, which are restricted to the local Universe. For instance, based on the MGS catalog and ALFALFA Hi galaxy survey, previous studies (e.g. Dutta et al. 2020) have explored the relation between the HiMF and the galaxies with different colors. Future HiIM surveys could expand this study with the assistance of the stacking analysis. With the stacking analysis, galaxy population classification relies on the galaxy property of an optically selected galaxy catalog. In this work, we focus on the HiMF dependency on the galaxy population classified from the color-magnitude plane.

The SDSS MGS includes galaxies with their properties spanning a significant range in the color-magnitude plane, where the color is the  $u - r$  color and magnitude is the SDSS  $r$ -band absolute magnitude. The  $u - r$  color has been shown to be an optimal separator for the red and blue galaxies (Strateva et al. 2001), which is defined as a locus in the color-magnitude space (Baldry et al. 2004),

$$c_{ur}(M_r) = 2.06 - 0.244 \tanh\left(\frac{M_r + 20.07}{1.09}\right). \quad (20)$$

The red/blue galaxy separator locus is shown as the red curve in Figure 2.

Following the processing in Dutta et al. (2020), we further split 23% blue galaxies, which have their  $u - r$  color approaching the lower end of the galaxy distribution in the color-magnitude space. Such galaxies are referring as bluer galaxies and the separator locus is chosen as a curve parallel to the red/blue separator. The blue/bluer separator locus is shown with the blue curve in Figure 2.

## 4. RESULTS AND DISCUSSION

### 4.1. Bayesian-stacking with MGS-like catalog

Using the MGS-like galaxy catalog as the position proxy, we consider the HiMF estimation by Bayesian-stacking the Hi flux from the simulation catalog. The observation effect, e.g. the beam-smearing effect, is ignored, and the uncertainty raised from the measurement noise is emphasized. We simulate the measurements with the three different galaxy sub-samples, e.g. the red, blue, and bluer galaxy samples as defined in Section 3.5, individually. The simulation results are shown in Figure 3.

The results with different FAST noise levels are shown in different panels, i.e. from the top to the bottom, the results correspond to the noise level of the pilot, deep-field, and ultra-deep-field drift-scan observation. In each panel, the HiMF measurements, as well as the noise level, for the red, blue, and bluer galaxy samples are shown in red, blue, and cyan colors, respectively.

The vertical dashed line shows the 5-times-noise-level equivalent Hi mass, estimated via Equation (2) assuming a mean redshift of 0.1. We take 2 MHz as an approximation to the mean frequency width of different galaxy subsamples.

The five-times noise level represents a significant detection threshold for Hi galaxy survey and it is pushed to the low-mass end with repeating drift-scan observations. Only galaxies that are bright in radio bands can be well cataloged via the Hi galaxy survey.

The color-filled regions show the 68% confidence intervals of the measurements. We also present the HiMF directly obtained with the Hi mass from the TNG simulation, i.e.  $\Phi_g$ , using the dot-marked curves to examine the measurement accuracy. The HiMF measurements are consistent with the  $\Phi_g$

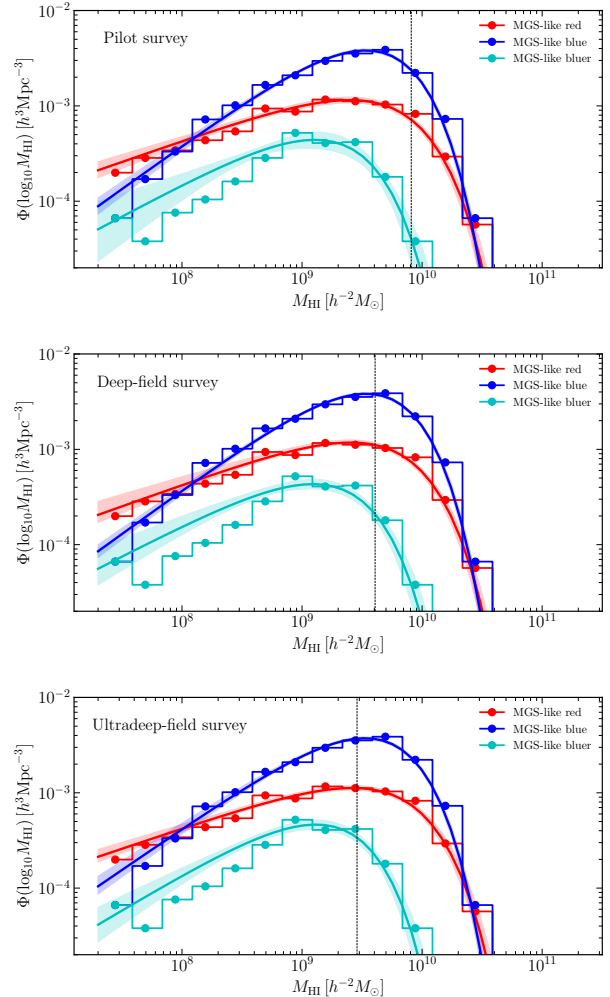


**Figure 3.** The HiMF estimated with the MGS-like sample. From top to bottom, different panels show the results with the noise level of the pilot, deep-field, and ultra-deep-field drift-scan observation, respectively (c.f. Table 2). In each panel, the HiMF estimated by Bayesian-stacking the red, blue, and bluer galaxy samples are shown with red, blue, and cyan colors, with the filled regions showing the 68% confidence interval. The dot-marked curves indicate the HiMF estimated directly using the galaxy Hi mass extracted from the simulated catalog, i.e.  $\Phi_g(M_{\text{HI}})$  as defined in Section 3.1. The vertical dashed lines indicate the Hi galaxy survey detection limit corresponding to 5 times observation noise r.m.s..

within the confidence intervals for all three galaxy subsamples. For each noise level injection, the Bayesian stacking method could significantly improve the HiMF measurements and constrain the HiMF even below the 5 times noise level, which estimates the detection limit for the Hi galaxy survey.

The FAST HiIM pilot and deep-field survey simulations assume a survey area of  $210 \text{ deg}^2$ . The simulation results show that the HiMF for both the red and blue galaxies can be well-constrained with the FAST HiIM pilot survey. However,

the HiMF for bluer galaxies needs the deep-field survey, which is 4 times repeating observations of the pilot survey.

We assume a survey area of  $210 \text{ deg}^2$  for the FAST HiIM pilot, deep-field, and ultra-deep-field surveys. The results for the pilot survey are shown in the top panel of Figure 3. The simulation results show that the HiMF for both the red and blue galaxies are well-constrained and consistent with  $\Phi_g$ , while the bluer galaxies' HiMF has slightly larger measurement uncertainty due to the limited samples in the bluer galaxy catalog.

The results for a FAST deep-field and ultra-deep-field survey are shown in the middle and bottom panel of Figure 3, respectively. The HiMF for each of the galaxy catalogs is well-constrained. Besides the bluer galaxy sample, the improvement in measurement uncertainty compared to the pilot survey is not significant. This indicates that the measurement noise is subdominant, especially for the red and blue galaxy samples, and the errors on the HiMF measurements are raised by the intrinsic scattering of the HiMF between different halos, i.e. the sample variance (Schneider 2008). The sample variance in HiMF measurements may indicate an environment-dependent HiMF, which requires conditional HiMF estimation (Li et al. 2022).

Instead of an ultra-deep-field survey, a wide-field survey is more efficient in beating down the sample variance. Generally speaking, with the same total observation time, a wide-field survey suffers from decreased sensitivity, which is tricky for traditional H I galaxy surveys. Beneficial from the Bayesian-stacking approach, the same sensitivity can be achieved by stacking a large number of samples distributed across a shallow but wide survey field, instead of an ultra-deep one. Such a wide-field survey can be quickly carried out with FAST drift-scan observation. For instance, if we assume that the galaxy number density is uniform across the sky, the noise level of the ultra-deep-field survey is equivalent to stacking galaxy samples over a survey area of  $\sim 1800 \text{ deg}^2$ . Currently, limited by the TNG simulation box size, performing a wide-field simulation is quite time-consuming. We will discuss the wide-field case further in future works.

The constrain results on the HiMF parameters for each case are listed in Table 3. All three parameters of red and blue populations can be well constrained with even a pilot survey. However, the parameters of the bluer galaxy catalog, which has limited galaxy samples, require a deep survey. We obtain a positive HiMF faint-end slope index,  $1 + \alpha$  for all the cases. Such HiMF represents an optically selected magnitude-limited sample that lacks faint galaxies. Indeed, when one gets closer to the mass resolution, the TNG simulation's sample completeness drops. The positive HiMF faint-end slope index may indicate a selection effect. Detailed discussions are shown in Section 4.4 with full galaxy samples.

**Table 3.** The HiMF parameter posterior distributions with MGS-like galaxy catalog.

	Pilot survey	Deep-field survey	Ultra-deep-field survey
Red galaxy catalog			
$\log_{10} \Phi_*$	$-2.99^{+0.05}_{-0.05}$	$-2.99^{+0.04}_{-0.05}$	$-3.00^{+0.03}_{-0.04}$
$\log_{10} M_*$	$9.82^{+0.06}_{-0.05}$	$9.81^{+0.05}_{-0.04}$	$9.87^{+0.05}_{-0.04}$
$\alpha$	$-0.59^{+0.06}_{-0.06}$	$-0.65^{+0.05}_{-0.08}$	$-0.62^{+0.04}_{-0.05}$
Blue galaxy catalog			
$\log_{10} \Phi_*$	$-2.35^{+0.02}_{-0.02}$	$-2.35^{+0.01}_{-0.02}$	$-2.38^{+0.02}_{-0.02}$
$\log_{10} M_*$	$9.59^{+0.02}_{-0.02}$	$9.57^{+0.02}_{-0.02}$	$9.61^{+0.02}_{-0.02}$
$\alpha$	$-0.14^{+0.05}_{-0.05}$	$-0.07^{+0.04}_{-0.04}$	$-0.20^{+0.05}_{-0.06}$
Bluer galaxy catalog			
$\log_{10} \Phi_*$	$-3.30^{+0.11}_{-0.15}$	$-3.32^{+0.07}_{-0.08}$	$-3.27^{+0.06}_{-0.07}$
$\log_{10} M_*$	$9.27^{+0.14}_{-0.12}$	$9.29^{+0.10}_{-0.08}$	$9.23^{+0.09}_{-0.08}$
$\alpha$	$-0.28^{+0.28}_{-0.25}$	$-0.40^{+0.14}_{-0.16}$	$-0.22^{+0.15}_{-0.15}$

#### 4.2. Flux confusion effect for MGS-like catalog

We further include the flux confusion effect using the MGS-like galaxy catalog by convolving the simulated H I sky cube with the FAST beam model. The results with the confusion effect are shown in the middle panel of Figure 4. As a comparison, the top panel shows the original HiMF estimation without the confusion effect. The results are all with the assumption of the FAST HiMF ultra-deep-field survey to minimize the measurement uncertainty from the noise.

The HiMF for each galaxy sample is shifted towards the high-mass end because of the H I flux of the galaxies within the beam resolution are mixed up. We adopt the confusion correction transfer function,  $T_{cc}$  (i.e. Equation (19)), to quantify the HiMF shift. The transfer functions are displayed in the bottom panel of Figure 4 and are estimated for each galaxy catalog separately. The errorbar for the transfer function is propagated from the measurements' uncertainty of the  $\Phi_B$  and  $\Phi_{ref}$ . The transfer function is below 1 at the low-mass end, where the red galaxy sample exhibits a transfer function closer to 1 compared to the blue and bluer galaxy samples, but the bluer galaxy shows a significant deviation from 1. It signifies a substantial influence of the confusion effects on HiMF estimates, particularly for blue and bluer galaxies, which primarily consist of satellite galaxies. The transfer function increases with the galaxy H I mass and eventually descends after a 'knee' mass, except for the bluer galaxy sample, which is noise-dominated at the high-mass end due to the absence of galaxy samples.

#### 4.3. The HiMF improvement with FAST HiIM

The constraint errors of the HiMF parameters with different FAST HiIM survey assumptions are listed in Table 4. The table contains  $1 \sigma$  HiMF parameter errors for red, blue, and bluer galaxy catalog from top to bottom. We list the errors of the deep-field survey (the left column), the ultra-deep-field

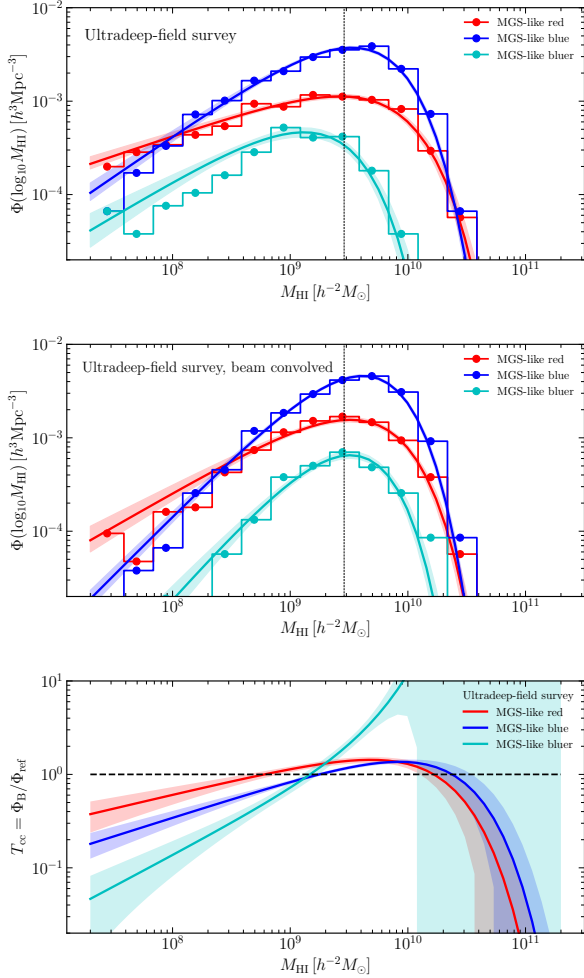


**Figure 4.** The HiMF measurements including the flux confusion effect. The results with/without flux confusion effect are shown in the top/middle panels. The bottom panel shows the confusion correction transfer function,  $T_{\text{cc}}$  (i.e. Equation (19)). The results for red, blue, and bluer galaxy catalogs are shown in red, blue, and cyan colors, respectively. All the results assume a FAST HiIM ultra-deep-field survey.

survey (the middle column), and the corresponding constraint errors with ALFALFA survey from Dutta et al. (2020) (the right column), respectively. In addition, in order to more intuitively observe the change of error with the integration time and compare the results with ALFALFA survey, we plot  $1\sigma$  errors of three main HiMF parameters in Fig. 5. The horizontal coordinate represents the FAST pilot survey, deep-field survey, and ultra-deep-field survey, respectively. The constraint errors of the red, blue, and bluer galaxies are shown in red, blue, and cyan, respectively. The dashed horizontal lines indicate the  $1\sigma$  errors of the HiMF parameters obtained by Dutta et al. (2020). Benefit from the high sensitivity of FAST, the constraint error with  $210 \text{ deg}^2$  of the pilot survey

**Table 4.** The HiMF parameter posterior distributions with MGS-like galaxy catalog compared with ALFALFA survey.

	Deep-field survey	Ultra-deep-field survey	ALFALFA <sup>†</sup>
Red galaxy catalog			
$\sigma(\log_{10} \Phi_*)$	0.045	0.035	0.055
$\sigma(\log_{10} M_*)$	0.045	0.045	0.040
$\sigma(\alpha)$	0.065	0.045	0.100
Blue galaxy catalog			
$\sigma(\log_{10} \Phi_*)$	0.015	0.020	0.029
$\sigma(\log_{10} M_*)$	0.020	0.020	0.030
$\sigma(\alpha)$	0.040	0.055	0.110
Bluer galaxy catalog			
$\sigma(\log_{10} \Phi_*)$	0.075	0.065	0.089
$\sigma(\log_{10} M_*)$	0.090	0.085	0.050
$\sigma(\alpha)$	0.155	0.150	0.380

<sup>†</sup> Parameter constraint results are from Dutta et al. 2020

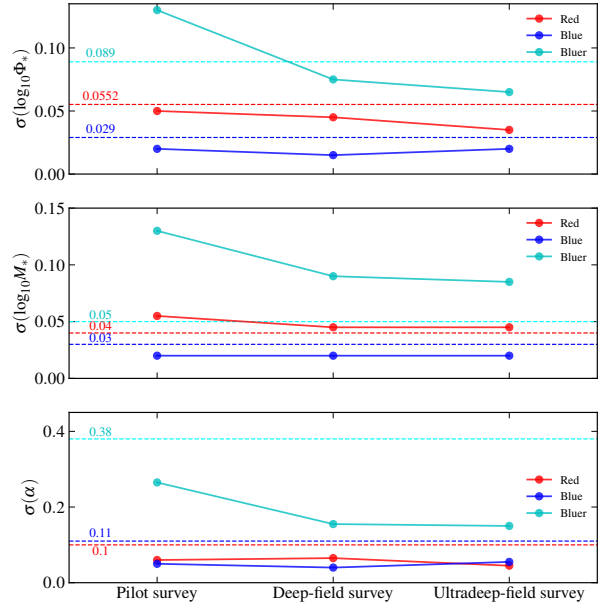


**Figure 5.** The HiMF parameter  $1\sigma$  errors of MGS-like galaxy catalog compared with ALFALFA survey.

is compatible with those obtained by the ALFALFA survey with nearly  $7000 \text{ deg}^2$ .

The constraint errors gradually decrease with deeper HiIM surveys, however, the error reduction is not significant. As mentioned above, we infer that the error of the sample is dominated by the sample variance, instead of the observational thermal noise. Due to the limited samples of the bluer galaxies, the constraint errors on  $M_*$  is generally greater than the current ALFALFA results. Therefore, rather than extend-

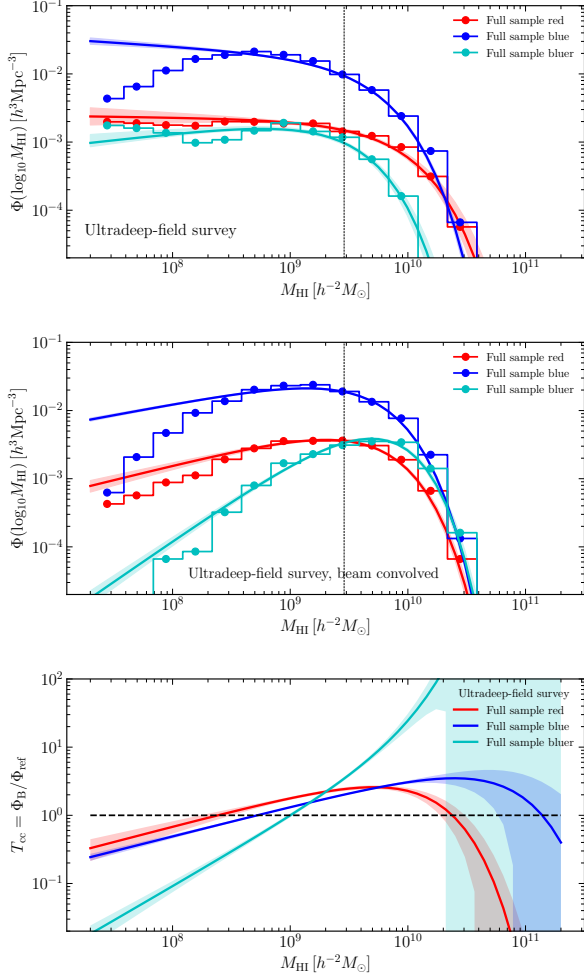


**Figure 6.** Same as Figure 4 but for the full galaxy sample.

ing the integration time, a large area survey would be ideal for stacking-based HiMF measurements.

#### 4.4. Selection completeness

The HiMF estimation is generally based on a volume-limited sample. Our simulation sky box is constructed with a snapshot and the initial galaxy sample is close to a volume-limited sample as the magnitude limit variation is negligible within the simulated comoving distance range.

We construct a full galaxy sample with all the galaxies identified in the TNG simulation snapshot and split it into red, blue, and bluer galaxy samples following the same partition method described in Section 3.5. Using the full galaxy sample and assuming with the ultra-deep-field survey, we apply the stacking-based HiMF estimation to the Hi cube without and with the beam confusion effect, respectively. The results are shown in Figure 6, where the top and middle panels show the results without and with beam confusion effect, respectively.

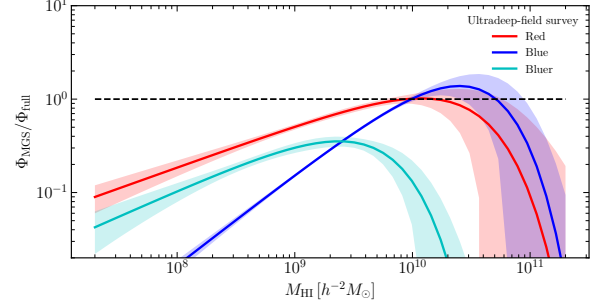


**Figure 7.** The HiMF ratio of the MGS-like sample with respect to the full sample, assuming the ultra-deep-field drift-scan observation. The results with the luminous red, blue, and bluer galaxy catalog are shown in red, blue, and cyan colors, respectively.

Without the beam confusion effect, the HiMF generally fits well with the Schechter function, except for the blue galaxy sample, which is significantly deviated from the Schechter function at the lower end of the HiMF. Such deviation may indicate an intrinsic incompleteness of the TNG galaxy sample with the galaxy’s stellar mass approaching the mass resolution of the simulation.

With the confusion effect, we observe a similar effect as the MGS, i.e. the HiMF is shifted towards the high-mass end. The confusion correction function for the full galaxy samples is shown in the bottom panel of Figure 6.

However, the stacking-based HiMF estimation is also affected by the completeness of the optically selected sample, in particular, the MGS-like galaxy sample, which is known to be a magnitude-limited sample (Strauss et al. 2002). We estimate the HiMF ratio of the MGS-like galaxy samples with respect to the full galaxy sample. The results are shown in Figure 7. The red, blue, and cyan colors represent the luminous red, blue, and bluer galaxies, respectively. The error represents the estimation uncertainty propagated from the measurement uncertainty of the HiMF. It is important to note that the accuracy of the transfer function decreases at the higher Hi mass end due to the smaller number of galaxies available in the sample. Both the red and blue galaxy subsamples exhibit transfer function values below unity at the lower Hi mass end, gradually approaching unity with Hi mass increases, and dropped at the higher-mass end. In contrast, the bluer galaxy subsample shows an increase in the transfer function with Hi mass but remains consistently below unity, even at the higher mass end. The deviation from unity indicates that there are galaxies are excluded with the optical selection magnitude limit, even with large Hi mass.

Notably, at the low Hi mass end, the blue galaxy subsample deviates more significantly from unity compared to the red galaxy subsample. This suggests that blue galaxies with lower Hi masses are less completely represented in the opti-

cally selected sample than red galaxies of comparable optical brightness.

The impact of sample completeness on the estimation of the HiMF has been discussed extensively in the literature. For example, in a series of studies on HiMF estimation using data from the ALFALFA Hi galaxy survey, the effects of sample completeness have been analyzed (Dutta & Khandai 2021; Dutta et al. 2022). Additionally, Li et al. (2022) proposed an Hi mass estimator that incorporates various galaxy properties to provide unbiased Hi mass estimates.

However, we emphasize that the sample completeness addressed in this work is fundamentally different from that considered in previous studies. Here, the completeness issue arises from the magnitude limit in the optical band, rather than the flux limit in radio observations. This distinction is particularly significant for Bayesian stacking-based HiMF estimation, which relies on optically selected galaxy samples. Since establishing strategies to limit the influence of optical selection effects is beyond the scope of this study, we defer this task to future research to enhance HiMF calculations.

## 5. CONCLUSION

In this work, we simulate the Bayesian-stacking-based HiMF estimation with FAST HiIM drift scan survey. Using one of the simulation snapshots of the TNG50, we simulated the Hi cube, as well as the corresponding optical galaxy survey catalog, at redshift of  $z \sim 0.1$ , which aligns with one of the RFI-free frequency band of FAST L-band.

Following the previous HiMF analysis (Dutta et al. 2020), we simulate galaxy catalog according to the galaxy selection criteria of the main galaxy sample (MGS) of SDSS Data Release 7, and split the MGS-like catalog into three subsamples, i.e. the red, blue, and bluer galaxy catalogs, based on the galaxy characteristics in the color-magnitude plane.

We also consider the observational thermal noise and the confusion effect caused by the FAST beam. Assuming the survey area of  $210 \text{ deg}^2$ , we simulate the HiIM survey with different observation integration time per beam, i.e., 29 s as the Pilot survey, 115 s as the Deep-field survey, and 230 s as the Ultradeep-field survey.

The HiMF can be effectively reconstructed using Bayesian-stacking-based HiMF estimation for the red, blue, and bluer galaxy catalogs, utilizing the observation integration times of the Pilot survey, Deep-field survey, and Ultradeep-field survey. Due to the limited sample amount, the HiMF recon-

struction error for bluer galaxy catalog is larger than the other two galaxy catalogs. The improvement of the constraint uncertainty with more integration time is not significant, which indicates currently HiMF estimation is sample variance dominated. A large field HiIM survey is efficient for reducing the sample variance and robust for Bayesian-stacking-based HiMF estimation.

We also find a significant confusion effect due to the limited angular resolution of the FAST beam. The confusion effect shifts the HiMF to the higher-mass end and thus may cause underestimation of the HiMF at the lower-mass end. With the simulation, we adopt a transfer function to characterize and correct the confusion effect for the red, blue, and bluer catalogs, respectively.

The effect caused by the sample incompleteness is notable in our simulation. An intrinsic incompleteness arises from the TNG galaxy sample when the stellar mass of the galaxies approaches the mass resolution limit. Besides, the Bayesian-stacking-based HiMF estimation is also affected by the completeness of the optically selected sample. With our simulation, we imply a transfer function to characterize the completeness effect for the MGS-like catalog for the red, blue, and bluer catalogs, respectively.

With this work, we highlight a few systematic effects for Bayesian-stacking-based HiMF estimation for current and future HiIM surveys with FAST. This study serves as a fundamental preparation for further HiMF analysis with our FAST drift scan surveys for HiIM.

## ACKNOWLEDGMENTS

We acknowledge the support of the National SKA Program of China (Nos. 2022SKA0110200, 2022SKA0110203, 2022SKA0110100, 2022SKA0110101), the National Natural Science Foundation of China (Nos. 12473091, 12473001, 12361141814), 111 Project (No. B16009), and the NSFC International (Regional) Cooperation and Exchange Project (No. 12361141814). We express our gratitude to ChatGPT for its assistance in refining the manuscript and enhancing the code to improve execution efficiency.

## DATA AVAILABILITY

The corresponding author is available to share the simulated data underlying this article upon reasonable request.

*Software:* ASTROPY (Astropy Collaboration et al. 2013, 2018, 2022), CORNER (Foreman-Mackey 2016), MULTINEST (Feroz et al. 2009)

## REFERENCES

- Abazajian, K. N., Adelman-McCarthy, J. K., Agüeros, M. A., et al. 2009, *The Astrophysical Journal Supplement Series*, 182, 543, doi: [10.1088/0067-0049/182/2/543](https://doi.org/10.1088/0067-0049/182/2/543)
- Amiri, M., Bandura, K., Chen, T., et al. 2023, *The Astrophysical Journal*, 947, 16, doi: [10.3847/1538-4357/acb13f](https://doi.org/10.3847/1538-4357/acb13f)

- Anderson, C. J., Luciw, N. J., Li, Y. C., et al. 2018, *Monthly Notices of the Royal Astronomical Society*, 476, 3382, doi: [10.1093/mnras/sty346](https://doi.org/10.1093/mnras/sty346)
- Ansari, R., Campagne, J. E., Colom, P., et al. 2012, *Astronomy and Astrophysics*, 540, A129, doi: [10.1051/0004-6361/201117837](https://doi.org/10.1051/0004-6361/201117837)
- Astropy Collaboration, Robitaille, T. P., Tollerud, E. J., et al. 2013, *Astronomy and Astrophysics*, 558, A33, doi: [10.1051/0004-6361/201322068](https://doi.org/10.1051/0004-6361/201322068)
- Astropy Collaboration, Price-Whelan, A. M., Sipőcz, B. M., et al. 2018, *The Astronomical Journal*, 156, 123, doi: [10.3847/1538-3881/aabc4f](https://doi.org/10.3847/1538-3881/aabc4f)
- Astropy Collaboration, Price-Whelan, A. M., Lim, P. L., et al. 2022, *The Astrophysical Journal*, 935, 167, doi: [10.3847/1538-4357/ac7c74](https://doi.org/10.3847/1538-4357/ac7c74)
- Bagla, J. S., Khandai, N., & Datta, K. K. 2010, *Monthly Notices of the Royal Astronomical Society*, 407, 567, doi: [10.1111/j.1365-2966.2010.16933.x](https://doi.org/10.1111/j.1365-2966.2010.16933.x)
- Baldry, I. K., Glazebrook, K., Brinkmann, J., et al. 2004, *The Astrophysical Journal*, 600, 681, doi: [10.1086/380092](https://doi.org/10.1086/380092)
- Bandura, K., Addison, G. E., Amiri, M., et al. 2014, *Society of Photo-Optical Instrumentation Engineers (SPIE) Conference Series*, Vol. 9145, *Canadian Hydrogen Intensity Mapping Experiment (CHIME) pathfinder*, 914522, doi: [10.1117/12.2054950](https://doi.org/10.1117/12.2054950)
- Barnes, D. G., Staveley-Smith, L., de Blok, W. J. G., et al. 2001, *Monthly Notices of the Royal Astronomical Society*, 322, 486, doi: [10.1046/j.1365-8711.2001.04102.x](https://doi.org/10.1046/j.1365-8711.2001.04102.x)
- Battye, R. A., Browne, I. W. A., Dickinson, C., et al. 2013, *Monthly Notices of the Royal Astronomical Society*, 434, 1239, doi: [10.1093/mnras/stt1082](https://doi.org/10.1093/mnras/stt1082)
- Blyth, S., Baker, A. J., Holwerda, B., et al. 2016, in *MeerKAT Science: On the Pathway to the SKA*, 4, doi: [10.22323/1.277.0004](https://doi.org/10.22323/1.277.0004)
- Bull, P., Ferreira, P. G., Patel, P., & Santos, M. G. 2015, *The Astrophysical Journal*, 803, 21, doi: [10.1088/0004-637X/803/1/21](https://doi.org/10.1088/0004-637X/803/1/21)
- Carucci, I. P., Bernal, J. L., Cunnington, S., et al. 2024, *arXiv e-prints*, arXiv:2412.06750, doi: [10.48550/arXiv.2412.06750](https://doi.org/10.48550/arXiv.2412.06750)
- Chang, T.-C., Pen, U.-L., Bandura, K., & Peterson, J. B. 2010, *Nature*, 466, 463, doi: [10.1038/nature09187](https://doi.org/10.1038/nature09187)
- Chang, T.-C., Pen, U.-L., Peterson, J. B., & McDonald, P. 2008, *Physical Review Letter*, 100, 091303, doi: [10.1103/PhysRevLett.100.091303](https://doi.org/10.1103/PhysRevLett.100.091303)
- Charlot, S., & Fall, S. M. 2000, *The Astrophysical Journal*, 539, 718, doi: [10.1086/309250](https://doi.org/10.1086/309250)
- Chen, X. 2012, in *International Journal of Modern Physics Conference Series*, Vol. 12, *International Journal of Modern Physics Conference Series*, 256–263, doi: [10.1142/S2010194512006459](https://doi.org/10.1142/S2010194512006459)
- Chen, Z., Chapman, E., Wolz, L., & Mazumder, A. 2023, *Monthly Notices of the Royal Astronomical Society*, 524, 3724, doi: [10.1093/mnras/stad2102](https://doi.org/10.1093/mnras/stad2102)
- Conroy, C., & Gunn, J. E. 2010, *The Astrophysical Journal*, 712, 833, doi: [10.1088/0004-637X/712/2/833](https://doi.org/10.1088/0004-637X/712/2/833)
- Conroy, C., Gunn, J. E., & White, M. 2009, *The Astrophysical Journal*, 699, 486, doi: [10.1088/0004-637X/699/1/486](https://doi.org/10.1088/0004-637X/699/1/486)
- Cunnington, S., Li, Y., Santos, M. G., et al. 2023, *Monthly Notices of the Royal Astronomical Society*, 518, 6262, doi: [10.1093/mnras/stac3060](https://doi.org/10.1093/mnras/stac3060)
- DeBoer, D. R., Gough, R. G., Bunton, J. D., et al. 2009, *Proceedings of the IEEE*, 97, 1507, doi: [10.1109/JPROC.2009.2016516](https://doi.org/10.1109/JPROC.2009.2016516)
- Delhaize, J., Meyer, M. J., Staveley-Smith, L., & Boyle, B. J. 2013, *Monthly Notices of the Royal Astronomical Society*, 433, 1398, doi: [10.1093/mnras/stt810](https://doi.org/10.1093/mnras/stt810)
- Deng, F., Gong, Y., Wang, Y., et al. 2022, *Monthly Notices of the Royal Astronomical Society*, 515, 5894, doi: [10.1093/mnras/stac2185](https://doi.org/10.1093/mnras/stac2185)
- Diemer, B., Stevens, A. R. H., Forbes, J. C., et al. 2018, *The Astrophysical Journal Supplement Series*, 238, 33, doi: [10.3847/1538-4365/aae387](https://doi.org/10.3847/1538-4365/aae387)
- Dutta, S., & Khandai, N. 2021, *Monthly Notices of the Royal Astronomical Society*, 500, L37, doi: [10.1093/mnras/slaa178](https://doi.org/10.1093/mnras/slaa178)
- Dutta, S., Khandai, N., & Dey, B. 2020, *Monthly Notices of the Royal Astronomical Society*, 494, 2664, doi: [10.1093/mnras/staa864](https://doi.org/10.1093/mnras/staa864)
- Dutta, S., Khandai, N., & Rana, S. 2022, *Monthly Notices of the Royal Astronomical Society*, 511, 2585, doi: [10.1093/mnras/stab3618](https://doi.org/10.1093/mnras/stab3618)
- Feroz, F., Hobson, M. P., & Bridges, M. 2009, *Monthly Notices of the Royal Astronomical Society*, 398, 1601, doi: [10.1111/j.1365-2966.2009.14548.x](https://doi.org/10.1111/j.1365-2966.2009.14548.x)
- Foreman-Mackey, D. 2016, *The Journal of Open Source Software*, 1, 24, doi: [10.21105/joss.00024](https://doi.org/10.21105/joss.00024)
- Gao, L.-Y., Li, Y., Ni, S., & Zhang, X. 2023, *Monthly Notices of the Royal Astronomical Society*, 525, 5278, doi: [10.1093/mnras/stad2646](https://doi.org/10.1093/mnras/stad2646)
- Giovanelli, R., Haynes, M. P., Kent, B. R., et al. 2005, *The Astronomical Journal*, 130, 2598, doi: [10.1086/497431](https://doi.org/10.1086/497431)
- Gnedin, N. Y., & Kravtsov, A. V. 2011, *The Astrophysical Journal*, 728, 88, doi: [10.1088/0004-637X/728/2/88](https://doi.org/10.1088/0004-637X/728/2/88)
- Holwerda, B. W., Blyth, S. L., & Baker, A. J. 2012, in *The Spectral Energy Distribution of Galaxies - SED 2011*, ed. R. J. Tuffs & C. C. Popescu, Vol. 284, 496–499, doi: [10.1017/S1743921312009702](https://doi.org/10.1017/S1743921312009702)
- Hu, W., Wang, X., Wu, F., et al. 2020, *Monthly Notices of the Royal Astronomical Society*, 493, 5854, doi: [10.1093/mnras/staa650](https://doi.org/10.1093/mnras/staa650)
- Jarvis, M., Taylor, R., Agudo, I., et al. 2016, in *MeerKAT Science: On the Pathway to the SKA*, 6, doi: [10.22323/1.277.0006](https://doi.org/10.22323/1.277.0006)

- Jiang, P., Tang, N.-Y., Hou, L.-G., et al. 2020, *Research in Astronomy and Astrophysics*, 20, 064, doi: [10.1088/1674-4527/20/5/64](https://doi.org/10.1088/1674-4527/20/5/64)
- Jin, S.-J., He, D.-Z., Xu, Y., Zhang, J.-F., & Zhang, X. 2020, *JCAP*, 03, 051, doi: [10.1088/1475-7516/2020/03/051](https://doi.org/10.1088/1475-7516/2020/03/051)
- Jin, S.-J., Wang, L.-F., Wu, P.-J., Zhang, J.-F., & Zhang, X. 2021, *Phys. Rev. D*, 104, 103507, doi: [10.1103/PhysRevD.104.103507](https://doi.org/10.1103/PhysRevD.104.103507)
- Johnston, S., Bailes, M., Bartel, N., et al. 2007, *Publications Astronomical Society of Australia*, 24, 174, doi: [10.1071/AS07033](https://doi.org/10.1071/AS07033)
- Jonas, J. L. 2009, *IEEE Proceedings*, 97, 1522, doi: [10.1109/JPROC.2009.2020713](https://doi.org/10.1109/JPROC.2009.2020713)
- Jones, M. G., Haynes, M. P., Giovanelli, R., & Moorman, C. 2018, *Monthly Notices of the Royal Astronomical Society*, 477, 2, doi: [10.1093/mnras/sty521](https://doi.org/10.1093/mnras/sty521)
- Koribalski, B. S., Staveley-Smith, L., Westmeier, T., et al. 2020, *Astrophysics and Space Science*, 365, 118, doi: [10.1007/s10509-020-03831-4](https://doi.org/10.1007/s10509-020-03831-4)
- Li, D., & Pan, Z. 2016, *Radio Science*, 51, 1060, doi: [10.1002/2015RS005877](https://doi.org/10.1002/2015RS005877)
- Li, D., Wang, P., Qian, L., et al. 2018, *IEEE Microwave Magazine*, 19, 112, doi: [10.1109/MMM.2018.2802178](https://doi.org/10.1109/MMM.2018.2802178)
- Li, J., Zuo, S., Wu, F., et al. 2020, *Science China Physics, Mechanics, and Astronomy*, 63, 129862, doi: [10.1007/s11433-020-1594-8](https://doi.org/10.1007/s11433-020-1594-8)
- Li, X., Li, C., Mo, H. J., Xiao, T., & Wang, J. 2022, *The Astrophysical Journal*, 941, 48, doi: [10.3847/1538-4357/ac9ccb](https://doi.org/10.3847/1538-4357/ac9ccb)
- Li, Y., Santos, M. G., Grainge, K., Harper, S., & Wang, J. 2021, *Monthly Notices of the Royal Astronomical Society*, 501, 4344, doi: [10.1093/mnras/staa3856](https://doi.org/10.1093/mnras/staa3856)
- Li, Y., Wang, Y., Deng, F., et al. 2023, *The Astrophysical Journal*, 954, 139, doi: [10.3847/1538-4357/ace896](https://doi.org/10.3847/1538-4357/ace896)
- Lidz, A., Furlanetto, S. R., Oh, S. P., et al. 2011, *The Astrophysical Journal*, 741, 70, doi: [10.1088/0004-637X/741/2/70](https://doi.org/10.1088/0004-637X/741/2/70)
- Liu, D., Li, Y., Tramonte, D., et al. 2024, arXiv e-prints, arXiv:2411.03988, doi: [10.48550/arXiv.2411.03988](https://doi.org/10.48550/arXiv.2411.03988)
- Loeb, A., & Wyithe, J. S. B. 2008, *Physical Review Letter*, 100, 161301, doi: [10.1103/PhysRevLett.100.161301](https://doi.org/10.1103/PhysRevLett.100.161301)
- Ma, W., Guo, H., Xu, H., et al. 2024, arXiv e-prints, arXiv:2411.09903, doi: [10.48550/arXiv.2411.09903](https://doi.org/10.48550/arXiv.2411.09903)
- Mao, Y., Tegmark, M., McQuinn, M., Zaldarriaga, M., & Zahn, O. 2008, *Physical Review D*, 78, 023529, doi: [10.1103/PhysRevD.78.023529](https://doi.org/10.1103/PhysRevD.78.023529)
- Martin, A. M., Papastergis, E., Giovanelli, R., et al. 2010, *The Astrophysical Journal*, 723, 1359, doi: [10.1088/0004-637X/723/2/1359](https://doi.org/10.1088/0004-637X/723/2/1359)
- Martin, A. M., Papastergis, E., Giovanelli, R., et al. 2010, *The Astrophysical Journal*, 723, 1359, doi: [10.1088/0004-637X/723/2/1359](https://doi.org/10.1088/0004-637X/723/2/1359)
- Masui, K. W., Switzer, E. R., Banavar, N., et al. 2013, *Astrophysical Journal Letters*, 763, L20, doi: [10.1088/2041-8205/763/1/L20](https://doi.org/10.1088/2041-8205/763/1/L20)
- MeerKLASS Collaboration, Barberi-Squarotti, M., Bernal, J. L., et al. 2024, arXiv e-prints, arXiv:2407.21626, doi: [10.48550/arXiv.2407.21626](https://doi.org/10.48550/arXiv.2407.21626)
- Meyer, M., Robotham, A., Obreschkow, D., et al. 2017, *Publications Astronomical Society of Australia*, 34, 52, doi: [10.1017/pasa.2017.31](https://doi.org/10.1017/pasa.2017.31)
- Nan, R., Li, D., Jin, C., et al. 2011, *International Journal of Modern Physics D*, 20, 989, doi: [10.1142/S0218271811019335](https://doi.org/10.1142/S0218271811019335)
- Nelson, D., Pillepich, A., Springel, V., et al. 2018, *Monthly Notices of the Royal Astronomical Society*, 475, 624, doi: [10.1093/mnras/stx3040](https://doi.org/10.1093/mnras/stx3040)
- Nelson, D., Springel, V., Pillepich, A., et al. 2019, *Computational Astrophysics and Cosmology*, 6, 2, doi: [10.1186/s40668-019-0028-x](https://doi.org/10.1186/s40668-019-0028-x)
- Newburgh, L. B., Bandura, K., Bucher, M. A., et al. 2016, *Society of Photo-Optical Instrumentation Engineers (SPIE) Conference Series*, Vol. 9906, HIRAX: a probe of dark energy and radio transients, 99065X, doi: [10.1117/12.2234286](https://doi.org/10.1117/12.2234286)
- Ni, S., Li, Y., Gao, L.-Y., & Zhang, X. 2022, *The Astrophysical Journal*, 934, 83, doi: [10.3847/1538-4357/ac7a34](https://doi.org/10.3847/1538-4357/ac7a34)
- Oosterloo, T., Verheijen, M. A. W., van Cappellen, W., et al. 2009, in *Wide Field Astronomy & Technology for the Square Kilometre Array*, 70, doi: [10.22323/1.132.0070](https://doi.org/10.22323/1.132.0070)
- Pan, H., Jarvis, M. J., Allison, J. R., et al. 2020, *Monthly Notices of the Royal Astronomical Society*, 491, 1227, doi: [10.1093/mnras/stz3030](https://doi.org/10.1093/mnras/stz3030)
- Pan, H., Jarvis, M. J., Ponomareva, A. A., et al. 2021, *Monthly Notices of the Royal Astronomical Society*, 508, 1897, doi: [10.1093/mnras/stab2601](https://doi.org/10.1093/mnras/stab2601)
- Pan, H., Jarvis, M. J., Zhu, M., et al. 2024, *Monthly Notices of the Royal Astronomical Society*, 534, 202, doi: [10.1093/mnras/stae2054](https://doi.org/10.1093/mnras/stae2054)
- Pan, J.-D., Wu, P.-J., Du, G.-H., Li, Y., & Zhang, X. 2024, <https://arxiv.org/abs/2408.00268>
- Paul, S., Santos, M. G., Chen, Z., & Wolz, L. 2023, arXiv e-prints, arXiv:2301.11943, doi: [10.48550/arXiv.2301.11943](https://doi.org/10.48550/arXiv.2301.11943)
- Paul, S., Santos, M. G., Townsend, J., et al. 2021, *Monthly Notices of the Royal Astronomical Society*, 505, 2039, doi: [10.1093/mnras/stab1089](https://doi.org/10.1093/mnras/stab1089)
- Perdereau, O., Ansari, R., Stebbins, A., et al. 2022, *Monthly Notices of the Royal Astronomical Society*, 517, 4637, doi: [10.1093/mnras/stac2832](https://doi.org/10.1093/mnras/stac2832)
- Peterson, J. B., Aleksan, R., Ansari, R., et al. 2009, in *astro2010: The Astronomy and Astrophysics Decadal Survey*, Vol. 2010, 234. <https://arxiv.org/abs/0902.3091>

- Planck Collaboration, Ade, P. A. R., Aghanim, N., et al. 2016, *Astronomy and Astrophysics*, 594, A13, doi: [10.1051/0004-6361/201525830](https://doi.org/10.1051/0004-6361/201525830)
- Pritchard, J. R., & Loeb, A. 2008, *Physical Review D*, 78, 103511, doi: [10.1103/PhysRevD.78.103511](https://doi.org/10.1103/PhysRevD.78.103511)
- Rhee, J. 2020, in *The Build-Up of Galaxies through Multiple Tracers and Facilities*, 18, doi: [10.5281/zenodo.3756456](https://doi.org/10.5281/zenodo.3756456)
- Rhee, J., Lah, P., Briggs, F. H., et al. 2018, *Monthly Notices of the Royal Astronomical Society*, 473, 1879, doi: [10.1093/mnras/stx2461](https://doi.org/10.1093/mnras/stx2461)
- Rosenberg, J. L., & Schneider, S. E. 2002, *The Astrophysical Journal*, 567, 247, doi: [10.1086/338377](https://doi.org/10.1086/338377)
- Ross, A. J., Samushia, L., Howlett, C., et al. 2015, *Monthly Notices of the Royal Astronomical Society*, 449, 835, doi: [10.1093/mnras/stv154](https://doi.org/10.1093/mnras/stv154)
- Santos, M., Bull, P., Alonso, D., et al. 2015, in *Advancing Astrophysics with the Square Kilometre Array (AASKA14)*, 19. <https://arxiv.org/abs/1501.03989>
- Santos, M. G., Cluver, M., Hilton, M., et al. 2017, arXiv e-prints, arXiv:1709.06099. <https://arxiv.org/abs/1709.06099>
- Scargle, J. D., Norris, J. P., Jackson, B., & Chiang, J. 2013, *The Astrophysical Journal*, 764, 167, doi: [10.1088/0004-637X/764/2/167](https://doi.org/10.1088/0004-637X/764/2/167)
- Schneider, S. E. 2008, in *Dark Galaxies and Lost Baryons*, ed. J. I. Davies & M. J. Disney, Vol. 244, 103–111, doi: [10.1017/S1743921307013889](https://doi.org/10.1017/S1743921307013889)
- Seo, H.-J., Dodelson, S., Marriner, J., et al. 2010, *The Astrophysical Journal*, 721, 164, doi: [10.1088/0004-637X/721/1/164](https://doi.org/10.1088/0004-637X/721/1/164)
- Square Kilometre Array Cosmology Science Working Group, Bacon, D. J., Battye, R. A., et al. 2020, *Publications Astronomical Society of Australia*, 37, e007, doi: [10.1017/pasa.2019.51](https://doi.org/10.1017/pasa.2019.51)
- Strateva, I., Ivezić, Ž., Knapp, G. R., et al. 2001, *The Astronomical Journal*, 122, 1861, doi: [10.1086/323301](https://doi.org/10.1086/323301)
- Strauss, M. A., Weinberg, D. H., Lupton, R. H., et al. 2002, *The Astronomical Journal*, 124, 1810, doi: [10.1086/342343](https://doi.org/10.1086/342343)
- Sun, S., Li, J., Wu, F., et al. 2022, *Research in Astronomy and Astrophysics*, 22, 065020, doi: [10.1088/1674-4527/ac684d](https://doi.org/10.1088/1674-4527/ac684d)
- Switzer, E. R., Masui, K. W., Bandura, K., et al. 2013, *Monthly Notices of the Royal Astronomical Society*, 434, L46, doi: [10.1093/mnras/slt074](https://doi.org/10.1093/mnras/slt074)
- Verheijen, M., Oosterloo, T., Heald, G., & van Cappellen, W. 2009, in *Panoramic Radio Astronomy: Wide-field 1-2 GHz Research on Galaxy Evolution*, 10, doi: [10.22323/1.089.0010](https://doi.org/10.22323/1.089.0010)
- Wang, J., Santos, M. G., Bull, P., et al. 2021, *Monthly Notices of the Royal Astronomical Society*, 505, 3698, doi: [10.1093/mnras/stab1365](https://doi.org/10.1093/mnras/stab1365)
- Wolz, L., Blake, C., Abdalla, F. B., et al. 2017, *Monthly Notices of the Royal Astronomical Society*, 464, 4938, doi: [10.1093/mnras/stw2556](https://doi.org/10.1093/mnras/stw2556)
- Wolz, L., Pourtsidou, A., Masui, K. W., et al. 2022, *Monthly Notices of the Royal Astronomical Society*, 510, 3495, doi: [10.1093/mnras/stab3621](https://doi.org/10.1093/mnras/stab3621)
- Wu, F., Li, J., Zuo, S., et al. 2021, *Monthly Notices of the Royal Astronomical Society*, 506, 3455, doi: [10.1093/mnras/stab1802](https://doi.org/10.1093/mnras/stab1802)
- Wu, P.-J., Li, Y., Zhang, J.-F., & Zhang, X. 2023, *Science China Physics, Mechanics, and Astronomy*, 66, 270413, doi: [10.1007/s11433-022-2104-7](https://doi.org/10.1007/s11433-022-2104-7)
- Wu, P.-J., Shao, Y., Jin, S.-J., & Zhang, X. 2023, *Journal of Cosmology and Astroparticle Physics*, 2023, 052, doi: [10.1088/1475-7516/2023/06/052](https://doi.org/10.1088/1475-7516/2023/06/052)
- Wu, P.-J., & Zhang, X. 2022, *JCAP*, 01, 060, doi: [10.1088/1475-7516/2022/01/060](https://doi.org/10.1088/1475-7516/2022/01/060)
- Wyithe, J. S. B., & Loeb, A. 2008, *Monthly Notices of the Royal Astronomical Society*, 383, 606, doi: [10.1111/j.1365-2966.2007.12568.x](https://doi.org/10.1111/j.1365-2966.2007.12568.x)
- Wyithe, J. S. B., Loeb, A., & Geil, P. M. 2008, *Monthly Notices of the Royal Astronomical Society*, 383, 1195, doi: [10.1111/j.1365-2966.2007.12631.x](https://doi.org/10.1111/j.1365-2966.2007.12631.x)
- Xu, Y., Wang, X., & Chen, X. 2015, *The Astrophysical Journal*, 798, 40, doi: [10.1088/0004-637X/798/1/40](https://doi.org/10.1088/0004-637X/798/1/40)
- Yang, W., Wolz, L., Li, Y., et al. 2024, arXiv e-prints, arXiv:2412.08173, doi: [10.48550/arXiv.2412.08173](https://doi.org/10.48550/arXiv.2412.08173)
- Zhang, C.-P., Zhu, M., Jiang, P., et al. 2024, *Science China Physics, Mechanics, and Astronomy*, 67, 219511, doi: [10.1007/s11433-023-2219-7](https://doi.org/10.1007/s11433-023-2219-7)
- Zhang, J.-F., Gao, L.-Y., He, D.-Z., & Zhang, X. 2019, *Phys. Lett. B*, 799, 135064, doi: [10.1016/j.physletb.2019.135064](https://doi.org/10.1016/j.physletb.2019.135064)
- Zhang, K., Wu, J., Li, D., et al. 2019, *Science China Physics, Mechanics, and Astronomy*, 62, 959506, doi: [10.1007/s11433-019-9383-y](https://doi.org/10.1007/s11433-019-9383-y)
- Zhang, M., Li, Y., Zhang, J.-F., & Zhang, X. 2023, *Monthly Notices of the Royal Astronomical Society*, 524, 2420, doi: [10.1093/mnras/stad2033](https://doi.org/10.1093/mnras/stad2033)
- Zhang, M., Wang, B., Wu, P.-J., et al. 2021, *Astrophys. J.*, 918, 56, doi: [10.3847/1538-4357/ac0ef5](https://doi.org/10.3847/1538-4357/ac0ef5)
- Zhao, X., Li, Y., Yang, W., et al. 2024, arXiv e-prints, arXiv:2412.02582, doi: [10.48550/arXiv.2412.02582](https://doi.org/10.48550/arXiv.2412.02582)
- Zwaan, M. A., Meyer, M. J., Staveley-Smith, L., & Webster, R. L. 2005, *Monthly Notices of the Royal Astronomical Society*, 359, L30, doi: [10.1111/j.1745-3933.2005.00029.x](https://doi.org/10.1111/j.1745-3933.2005.00029.x)